Synthesis of ilmenite-type ε-Mn_2O_3 and its properties

Sergey V. Ovsyannikov,[1,2,] Alexander A. Tsirlin,[3] Igor V. Korobeynikov,[4] Natalia V. Morozova,[4] Alena A. Aslandukova,[1] Gerd Steinle-Neumann,[1] Stella Chariton,[5] Saiana Khandarkhaeva,[6] Konstantin Glazyrin,[7] Fabrice Wilhelm,[8] Andrei Rogalev,[8] and Leonid Dubrovinsky[1]*

[1] Bayerisches Geoinstitut, Universität Bayreuth, Universitätsstrasse 30, 95440 Bayreuth, Germany

[2] Institute for Solid State Chemistry of Ural Branch of Russian Academy of Sciences, 91 Pervomayskaya Str., Yekaterinburg 620219, Russia

[3] Experimental Physics VI, Center for Electronic Correlations and Magnetism, Institute of Physics, University of Augsburg, 86135 Augsburg, Germany

[4] M. N. Miheev Institute of Metal Physics of Ural Branch of Russian Academy of Sciences, 18 S. Kovalevskaya Str., Yekaterinburg 620137, Russia

[5] University of Chicago, Center for Advanced Radiation Sources, Chicago, IL 60637 USA

[6] Material Physics and Technology at Extreme Conditions, Laboratory of Crystallography, Universität Bayreuth, 95440 Bayreuth, Germany

[7] Photon Science, Deutsches Elektronen-Synchrotron, Notkestrasse 85, 22607 Hamburg, Germany

[8] European Synchrotron Radiation Facility, 71, avenue des Martyrs CS 40220, 38043 Grenoble Cedex 9, France

ABSTRACT In contrast to the corundum-type A_2X_3 structure, which has only one crystallographic site available for trivalent cations (e.g., in hematite), the closely related ABX_3 ilmenite-type structure comprises two different octahedrally-coordinated positions that are usually filled with differently charged ions (e.g., in $Fe^{2+}Ti^{4+}O_3$ ilmenite). Here, we report a synthesis of the first binary ilmenite-type compound fabricated from a simple transition metal oxide (Mn_2O_3) at high-pressure high-temperature (HP-HT) conditions. We experimentally established that at normal conditions the ilmenite-type $Mn^{2+}Mn^{4+}O_3$ (ε-Mn_2O_3) is an *n*-type semiconductor with an indirect narrow band gap of E_g=0.55 eV. Comparative investigations of the electronic properties of ε-Mn_2O_3 and previously discovered quadruple perovskite ζ-Mn_2O_3 phase, were carried out using X-ray absorption near edge spectroscopy (XANES). Magnetic susceptibility measurements reveal antiferromagnetic ordering in ε-Mn_2O_3 below 210 K. The synthesis of ε-Mn_2O_3 indicates that HP-HT conditions can induce charge disproportionation in simple transition metal oxides M_2O_3, and potentially various mixed-valence polymorphs of these oxides, e.g., with ilmenite-type, $LiNbO_3$-type, perovskite-type, and other structures, could be stabilized at HP-HT conditions.

I. INTRODUCTION

Manganese oxides display a range of unique physical and chemical properties and play an important role in basic sciences and in numerous industrial processes and devices. For instance, they are promising materials for applications in diverse magnetic technologies,[1-5] for catalysis,[6,7] for supercapacitor electrodes,[8] for lithium storage and alkaline battery applications,[9-11] and for other goals.[12-15] Various Mn-rich oxides, such as manganite perovskites, $A_{1-x}B_xMnO_3$,[16] more complex quadruple perovskites, e.g., AMn_7O_{12}[17-27] and many others[28-36] demonstrate interesting and often industry-relevant characteristics. Hence, synthesis of novel, chemically-simple, inexpensive and functional manganese oxides could uncover yet unknown scientific and industrial potentials.

Recent investigations of simple oxides of another transition metal, iron, revealed that using high pressures and high temperature (HP-HT) one can synthesize novel phases with unconventional stoichiometries, like Fe_4O_5,[37] Fe_5O_6,[38] $Fe_{13}O_{19}$,[39] Fe_7O_9,[40] Fe_9O_{11},[41] Fe_5O_7,[42] $Fe_{25}O_{32}$.[42] Some of these polymorphs can be quenched from HP-HT and stabilized at ambient conditions, opening up prospects for their academic investigations and potential industrial use. Note, for example, that the most common mixed-valence iron oxides, Fe_4O_5 and Fe_5O_6, were found to undergo spectacular charge-ordering-related phase transitions.[43-45] These findings along with the well-known Verwey transition in magnetite studied before,[46,47] contributed to a better understanding of physical properties of transition metal oxides.

However, in the case of chemically-simple manganese oxides, only a few novel mixed-valence phases with unconventional stoichiometries were reported to date, namely, Mn_5O_8 that was proposed as an effective catalyst,[48-50] and Mn_5O_7 that was observed *in-situ* at very high pressures.[51] On the other hand, it was found that the high-pressure polymorphs of some common manganese oxides can be readily recovered at ambient conditions, and can be of

significant interest because of their mixed-valence nature. In particular, a high-pressure *Pbcm* polymorph of Mn_3O_4 was found to be quenchable and stable at ambient conditions.[52-54] The trivalent cubic-bixbyite α-Mn_2O_3[55] demonstrated a diverse high-pressure behavior consisting of transformations to different perovskite-like structures[51,56-59] and to *Cmcm* post-perovskite.[60] One of the mixed-valence polymorphs of Mn_2O_3 with the quadruple perovskite structure (labeled as ζ-Mn_2O_3) was recovered at ambient conditions,[56] and has shown exceptionally promising semiconducting properties (e.g., a direct band gap of about 0.5 eV)[61] and a spin-induced multiferroicity below 50 K.[62,63] A further polymorph of Mn_2O_3 was synthesized at HP-HT conditions and tentatively assigned to a corundum-type phase labeled as ε-Mn_2O_3, but remained unexplored to date.[56]

In the present work, we synthesized single crystals of ε-Mn_2O_3. Using single-crystal X-ray diffraction we established that ε-Mn_2O_3 crystallizes in the ilmenite-type crystal structure that contains Mn ions in two different oxidation states, +2 and +4. To date, ilmenite-type structures were not observed in any simple binary oxides,[64-66] but were reported for multi-cation oxides, in which disproportional charge distribution is common.[67] We also report electronic and magnetic properties of ilmenite-type ε-Mn_2O_3.

II. EXPERIMENT

Preparation and characterization of samples

The samples of ilmenite-type ε-Mn_2O_3 were synthesized at HP-HT conditions using the multi-anvil presses at Bayerisches Geoinstitut (BGI).[68] We conducted the syntheses at different HP-HT conditions and found that relatively large single-crystalline samples of the

pure ilmenite-type phase can be obtained at pressures of ~16-17 GPa and temperatures of 1500 K or above. The typical synthesis times varied between 20 and 24 hours. We employed a standard multi-anvil assembly that included an octahedral container, inside which we assembled a cylindrical sample capsule made of a thin gold foil, a $LaCrO_3$ heater, the MgO insulating cylinders, and the W3Re/W25Re thermocouples. The synthesis procedure was similar to those described in previous publications.[69,70] Selected samples were examined by scanning electron microscopy (SEM) using a ZEISS LEO-1530 instrument. A phase analysis of the samples was performed using X-ray diffraction (XRD) studies using a high-brilliance Rigaku diffractometer.

Single-crystal X-ray diffraction and analysis

Single-crystal X-ray diffraction datasets of the selected crystals were acquired at BGI at ambient conditions, using a high-brilliance Bruker diffractometer (Ag K_α radiation) equipped with Osmic focusing X-ray optics and Apex CCD detector. We solved the crystal structure with the assistance of the SHELXT structure solution software[71] using intrinsic phasing, and refined with the Jana 2006 software.[72] CSD-XXXXXX contains the supplementary crystallographic data for this manuscript. These data can be obtained free of charge from FIZ Karlsruhe via https://www.ccdc.cam.ac.uk/structures/.

We analyzed the Mn-O bond lengths in the ilmenite-type ε-Mn_2O_3 phase using the common bond valence sums (BVS) method.[73] In the BVS method, a bond valence of each cation-anion chemical bond is determined as $s_{ij}=\exp[(R_{ij}-d_{ij})/b_0]$, where d_{ij} is the distance between atoms i and j, R_{ij} is the empirical bond valence parameter for this cation-anion pair (Mn-O in our case), and b_0 is an empirical parameter of about 0.37 Å. Then, the total BVS value of an ion is

determined as a sum of bond valences ($V_i = \sum_j s_{ij}$).[73] Taking into account three possible oxidation states of the Mn cations in this oxide (+2, +3, and +4), we performed the calculations of the BVS values for three bond-valence parameters R_{ij} as 1.790, 1.760, and 1.753 Å, which were determined at ambient conditions for Mn^{2+}–O, Mn^{3+}–O, and Mn^{4+}–O bonds, respectively.[73] The BVS values obtained in these calculations were renormalized accordingly to keep the charge balance in the sample as Mn_2O_3 stoichiometry.

Magnetic measurements

Magnetic susceptibility was measured on batches of small randomly oriented single crystals with a total mass of 6-7 mg. The data were collected in the temperature range of 1.8-400 K in applied fields up to 7 T using the MPMS3 SQUID magnetometer from Quantum Design.

XANES measurements

The X-ray absorption near edge spectra (XANES) were recorded at ID12 beamline of the ESRF (Grenoble, France) using total fluorescence yield detection mode in a back-scattering geometry.[74] For experiments at the Mn *K*-edge, we have used the second harmonic of HELIOS-II (λ_U=52mm) helical undulator. To reduce the heat load on the optical elements of the beamline, 8μm thick Al foil was inserted directly behind the primary slits. The intensity of the fundamental harmonic spectrum was reduced by a factor of 4. The double-crystal fixed-exit monochromator equipped with a pair of Si<111> crystals cooled down to −140 ºC was exploited. Given the ultra-low emittance of the source, we checked that the energy resolution of Si<111> monochromator at the Mn K-edge was close to the theoretical limit:

0.96 eV; whereas, the broadening due to finite lifetime of the 1s core-hole was 1.1 eV. We acquired the XANES spectra of not only ilmenite-type ε-Mn_2O_3 phase, but also of another high-pressure polymorph, ζ-Mn_2O_3 with a quadrupole-perovskite structure, whose electronic, magnetic, and other properties were already studied.[56,61-63] For comparison, we also recorded XANES spectra of α-Mn_2O_3, MnO and β-MnO_2.

Optical absorption spectroscopy

We selected four crystals of ε-Mn_2O_3 with typical sizes of 300-500 μm and polished them on both sides to the thickness of about 20 μm. The absorption spectroscopy measurements were carried out in the mid-infrared range using a Bruker IFS 120 Fourier transform spectrometer.[61] The absorption spectra acquired for these four samples were virtually identical.

Measurements of electronic transport properties under high pressure

Electrical resistance and the Seebeck coefficient (thermoelectric power) were measured under applied pressure up to 9 GPa at room temperature for single-crystalline samples of ε-Mn_2O_3. This study was accomplished using a mini-press setup that smoothly generated a force applied to a high-pressure cell and automatically measured and recorded all output signals; the sample was compressed in an anvil-type high-pressure cell of a modified Bridgman-type with the hemispherically-concave anvils.[75] A toroidal limestone container for the sample served both as a gasket and a pressure-transmitting medium.[76] The measurements were performed for two samples with the size of about 150×150×150 μm^3;[77] other details were the same as reported elsewhere.[76,77]

Density functional theory calculations

To support the experimental findings, we performed density functional theory (DFT) band-structure calculations using the FPLO code[78] with the Perdew-Burke-Ernzerhof exchange-correlation potential.[79] Strong correlations in the Mn 3*d* shell were taken into account on the mean-field level within the DFT+*U* scheme using the on-site Coulomb repulsion potential U = 3.5 eV, Hund's coupling J = 0.5 eV, and double-counting correction in the atomic limit. This choice of U and J is compatible with $U - J$ = 3 eV reported for Mn oxides previously.[80] All calculations were converged with the 8x8x8 Monkhorst-Pack k-point grid.

III. RESULTS AND DISCUSSION

In this work, we investigated a pressure-temperature (P-T) phase diagram of Mn_2O_3 in detail to determine the HP-HT conditions, at which ilmenite-type ε-Mn_2O_3 phase can be synthesized. We investigated magnetic properties of this phase by temperature-dependent measurements of magnetic susceptibility and magnetization. We also examined the electronic properties of this novel polymorph by several techniques, which included XANES, near-infrared absorption spectroscopy, electrical resistivity, and thermoelectric power measurements.

Ilmenite-type crystal structure

The crystal structure of ε-Mn_2O_3 at ambient conditions was solved for several microscopic single-crystalline grains. We found that ε-Mn_2O_3 adopts an ilmenite-type structure with the

rhombohedral $R\bar{3}$ symmetry (space group #148) (Figure 1). The typical unit cell parameters of this structure at normal conditions were determined as follows: a=5.0148(8) Å, c=14.1141(28) Å, V=307.39(11) Å^3, and Z=6. A calculated density of this phase is 5.114 g/cm^3. This value is about 2% higher than that in conventional cubic-bixbyite phase α-Mn_2O_3.[55] By diffraction methods we found no deviation in the stoichiometry in the crystals investigated. Other parameters of the ε-Mn_2O_3 structure are summarized in Table 1. A crystallographic information file (CIF) for the ilmenite-type Mn_2O_3 is provided in Supporting Information.

The ilmenite-type structure is similar to the more common corundum-type structure, but comprises two different octahedrally-coordinated crystallographic sites that may be filled with cations of different sizes (small tetravalent and large divalent). Using the common bond valence sums (BVS) method[73] (see Experiment Section) we determined the average oxidation states for the cations occupying Mn1 and Mn2 sites as +4.05 and +1.95, respectively (Figure 1). Volumes of the oxygen octahedra of Mn1 and Mn2 atoms in the structure of ε-Mn_2O_3 are 9.25 Å^3 and 12.80 Å^3, respectively. The significant difference in the volumes also corroborates the charge disproportionation between Mn1 and Mn2 sites. For comparison, we analyzed an “octahedron volume – oxidation state” relationship for a dozen of binary and

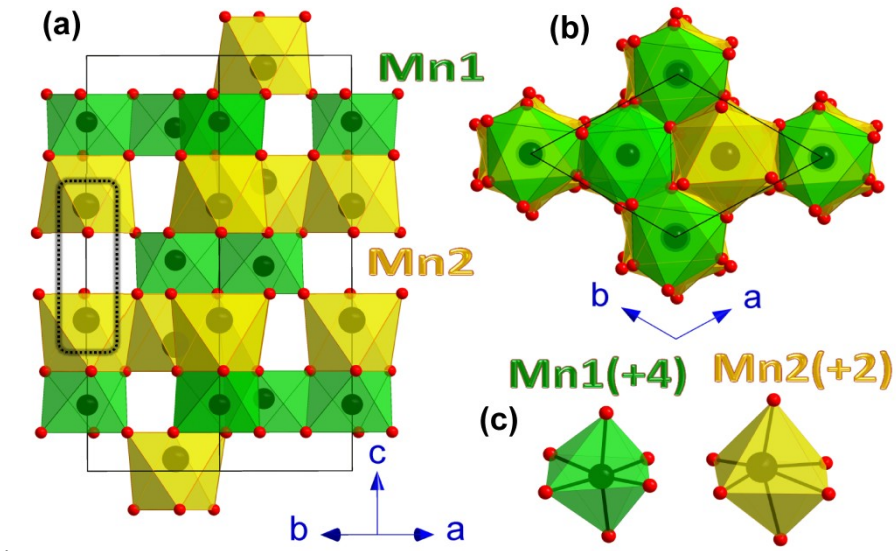

Figure 1. (*a*, *b*) Crystal structure of ilmenite-type ε-Mn_2O_3 at ambient conditions in two different projections. (*c*) The oxygen octahedra of Mn1 and Mn2 atoms.

ternary manganese oxides at ambient conditions in which the oxidation states of octahedral Mn cations are well known and vary between +2 and +4 (Figure 2). In particular, we considered high-quality data from FIZ Karlsruhe database (via https://www.ccdc.cam.ac.uk/structures/) for the ternary oxides containing Na^{+}, Li^{+}, Ca^{2+}, Mg^{2+}, La^{3+}, and Ti^{4+}. This analysis shows that octahedron volume strongly depends on average oxidation state of Mn, providing additional support of charge disproportionation reaction between Mn1 and Mn2 sites in the structure of ε-Mn_2O_3 (Figure 2). We found that the ilmenite-type ε-Mn_2O_3 is structurally similar to the ilmenite-type $Mn^{2+}Ti^{4+}O_3$ in which the Mn^{2+} and Ti^{4+} have a comparable sizable difference in volumes of oxygen octahedra (13.35 $Å^3$ vs 9.97 $Å^3$, respectively).[81] DFT calculations revealed the drastically different magnetic moments of 2.8 μ_B on Mn1 and 4.9 μ_B on Mn2, thus further supporting the oxidation states of +4 ($3d^3$) and +2 ($3d^5$), respectively.

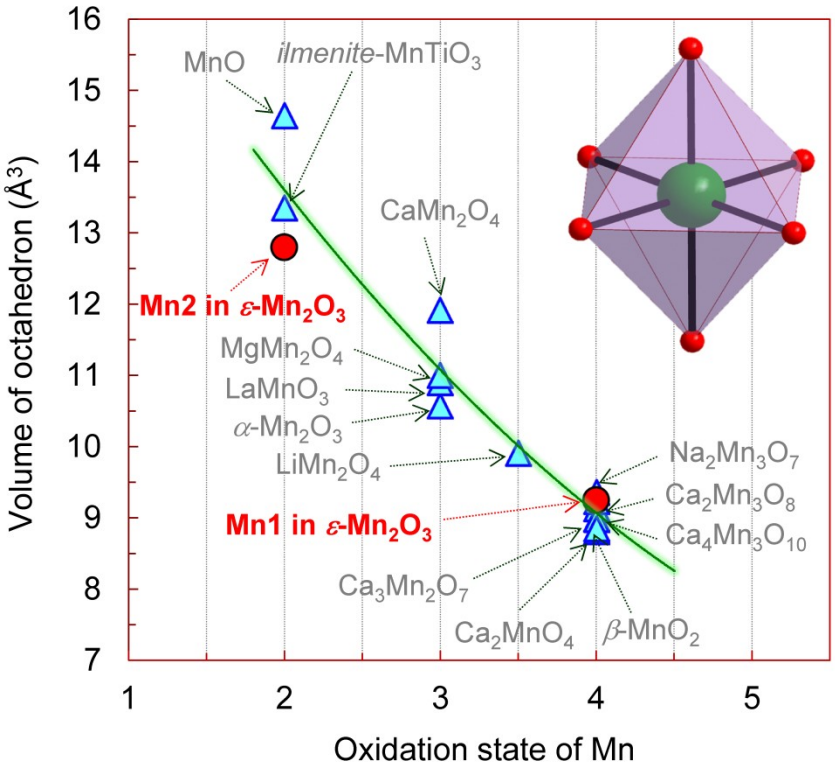

Figure 2. Dependence of volumes of coordination octahedra on oxidation state for Mn ions at ambient conditions, determined for manganese oxides with well-known oxidation states of cations, e.g., for oxides containing Na^{+}, Li^{+}, Ca^{2+}, Mg^{2+}, La^{3+}, and Ti^{4+} cations. We considered high-quality data from FIZ Karlsruhe database (https://www.ccdc.cam.ac.uk/structures/). Our data for Mn1 and Mn2 octahedra in the structure of ilmenite-type ε-Mn_2O_3 are shown by red symbols. The solid line serves as a guide to the eye.

As seen in Figure 1c, the divalent Mn2 cations are strongly displaced from the center of their coordination octahedra. However, these displacements compensate each other in pairs (one pair is highlighted by the black rectangle in Figure 1a), and hence, potential spontaneous electrical polarization in this structure for undoped stoichiometric Mn_2O_3 should be suppressed. The thermal displacements (parameters U) of Mn2 atoms were found to be strongly anisotropic (Table 1), and their maximal magnitude (U_{33}=0.0231 Å^2) was along the c-axis.

Thus, Mn_2O_3 is the first case among the simple transition metal oxides that can be stabilized in the ilmenite-type structure due to the charge distribution ($2Mn^{3+} \rightarrow Mn^{2+} + Mn^{4+}$), which is, moreover, well conserved at ambient conditions. Earlier theoretical investigations already considered charge-disproportionation reactions in Mn^{3+}-bearing materials,[82,83] with the goal to find general rules for the emergence of critical phenomena such as charge density waves, superconductivity, or spin density waves. These studies concluded that they are possible in materials with negative effective correlation energy U.[82,83] Further, two possible mechanisms that can result in negative energy U, were proposed:[83] The first one is exchange correlation which can be realized in 3d transition metals with either d^4 or d^6 electrons in the course of charge disproportionation ($2d^n \rightarrow d^{n-1} + d^{n+1}$).[83] The second mechanism is charge excitation which is potentially feasible in materials with either s^1 or d^9 electrons.[83] Given possible oxidation states, the above mechanisms are likely to occur only for $Mn^{3+}(3d^4)$, $Fe^{2+}(3d^6)$, $Co^{3+}(3d^6)$, or $Cu^{2+}(3d^9)$.[83] It is worth pointing out in this context that in the perovskite-type ζ-Mn_2O_3 phase, synthesized at similar HP-HT conditions but at a bit higher pressures (Figure 3), a group of Mn^{3+} ions was subjected to the charge disproportionation ($2Mn^{3+} \rightarrow Mn^{2+} + Mn^{4+}$), resulting in the doubling of the lattice parameter of the pseudo-cubic crystal structure and a slight triclinic distortion features[56] that suggest the emergence of a charge density wave.[61] Thus, the case of the ilmenite-type ε-Mn_2O_3 seems to be in line with these previous findings.[56,61] It appears that under moderate applied pressure, Mn_2O_3 tends to transform to a corundum-like structure, which is common for oxides of rather light transition metals like Fe, V, Cr, and Ti,[84] but simultaneously, the Mn^{3+} ions are subjected to the charge disproportionation and ordering. Thus, these two counteracting factors are likely responsible for the formation of the ilmenite-type structure.

The example of Mn_2O_3 shows that using a HP-HT technique one can convert simple manganese oxides to a mixed-valence state without any variations in both chemical

composition and stoichiometry. Thus, one can propose that the potential existence of a family of mixed-valence manganese oxides is pioneered by HP-HT synthesis, in analogy to iron oxides that are known to form multiple mixed-valence polymorphs, including those with the common Fe_2O_3 stoichiometry,[42] and various unconventional stoichiometries.[37-42]

Pressure-temperature phase diagram

A pressure-temperature phase diagram of Mn_2O_3 was experimentally determined in our previous work focused on the synthesis of quadruple perovskite ζ-Mn_2O_3.[56] Here, we explored the P-T region where ε-Mn_2O_3 is expected to be stable, and simultaneously searched for optimal conditions for the synthesis of its single crystals (Figure 3). Below 10 GPa, no phase transitions in Mn_2O_3 were detected, in agreement with previous HP-HT studies,[85] and, hence, this part of the P-T diagram is omitted here; two ambient-pressure phases, low-temperature β-Mn_2O_3 with an orthorhombically-distorted bixbyite-like structure,[86] and γ-Mn_2O_3 with a tetragonal spinel-like structure,[87,88] are not shown in this diagram.

The lower temperature boundaries separating the ambient-pressure cubic-bixbyite α-Mn_2O_3 phase from the ilmenite-type ε-Mn_2O_3 and from the previously reported quadruple perovskite ζ-Mn_2O_3 are significantly shifted relative to each other (Figure 3). This finding suggests that a kinetic barrier for the α-Mn_2O_3 → ε-Mn_2O_3 transformation is higher than that for α-Mn_2O_3 → ζ-Mn_2O_3 (Figure 3). This difference can be explained by the fact that the former requires a complete disproportionation of the Mn^{3+} charges ($2Mn^{3+} \rightarrow Mn^{2+} + Mn^{4+}$), whereas the latter transition involves only a partial charge transfer for about 30% of the Mn^{3+} ions.[56] The upper temperature "boundary" between ilmenite-type ε-Mn_2O_3 and high-pressure *Pbcm*-Mn_3O_4 phase reflects the fact that Mn_2O_3 tends to reduce to Mn_3O_4 at high temperatures, but this process strongly depends on synthesis conditions, such as oxygen fugacity (Figure 3).

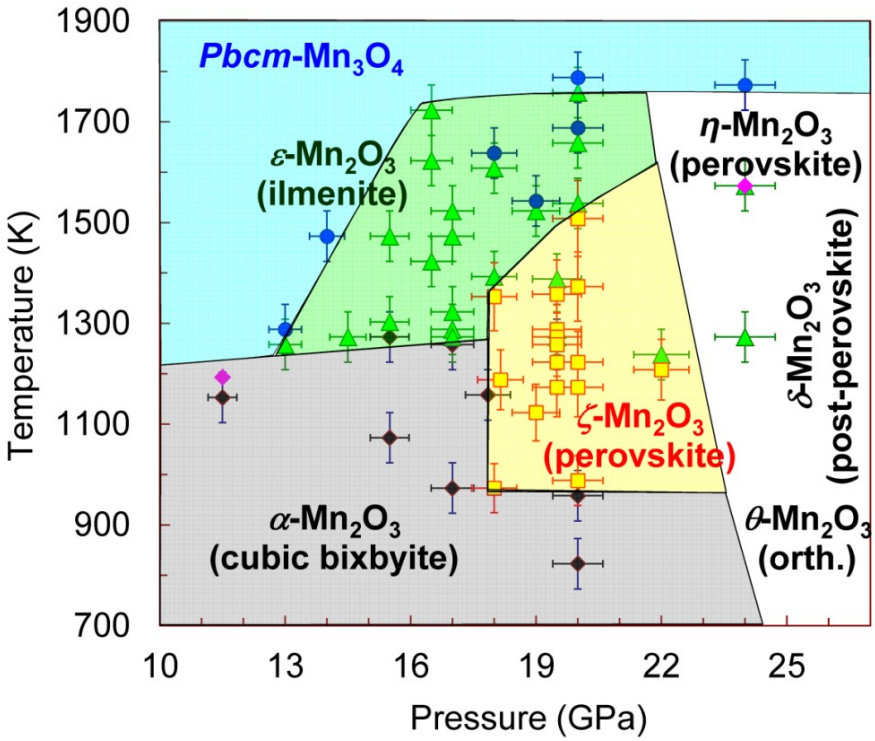

Figure 3. Pressure-temperature phase diagram of Mn_2O_3 established by HP-HT synthesis experiments. The boundaries between ilmenite-type ε-Mn_2O_3, cubic-bixbyite-type α-Mn_2O_3, and perovskite-type ζ-Mn_2O_3 phases depend on pressure-temperature conditions only. The high-temperature boundary between Mn_2O_3 and Mn_3O_4 is very sensitive to the oxygen fugacity conditions during HP-HT synthesis. Above 22-23 GPa at high temperatures, Mn_2O_3 was found to undergo a further phase transitions. These high-pressure phases were unquenchable to ambient conditions, and the recovered samples were crumbling powders with ilmenite-like structures. According to the literature, several phases can appear in the high pressure region, namely, perovskite-type η-Mn_2O_3,[57,51] post-perovskite-type δ-Mn_2O_3,[60] and orthorhombically-distorted θ-Mn_2O_3 phase.[58,59] Room-temperature studies documented a monoclinic distortion in the structure above 18 GPa.[89]

At synthesis pressures above 22-23 GPa and moderately high temperatures, the Mn_2O_3 samples were subjected to one more phase transition (Figure 3). Previous room-temperature and high-temperature X-ray diffraction studies reported several additional phases above 24-27 GPa, namely, a perovskite-like phase,[51,57] whose crystal structure differed from that of ζ-Mn_2O_3,[56] and hence could be named as η-Mn_2O_3, an orthorhombically-distorted phase (θ-Mn_2O_3),[58,59] and the post-perovskite δ-Mn_2O_3 phase with *Cmcm* symmetry discovered much earlier (Figure 3).[60] Other room-temperature structural and vibrational studies documented a

monoclinic distortion in the structure of Mn_2O_3 above 18 GPa,[89] and moderate changes in Raman spectra of Mn_2O_3 in the pressure range of 16-24 GPa,[90] respectively. The above-discussed phases were reported to be unquenchable to ambient conditions.[51,58-60]

In our experiments, the samples synthesized at pressures above 24 GPa appeared as crumbling powdery brown-colored pellets that were apparently formed on the decompression cycles. These recovered samples also had the ilmenite-like crystal structure. It seems plausible that, because the high-pressure phases of Mn_2O_3 (e.g., η-Mn_2O_3 and θ-Mn_2O_3) containing Mn^{2+} and Mn^{4+} ions are unquenchable to ambient conditions, upon decompression they turn into the lower-pressure phase in which Mn ions the same oxidation state (i.e., ilmenite ε-Mn_2O_3 phase). This appears plausible as in $Fe^{2+}Ti^{4+}O_3$, the ilmenite prototype, $Fe^{2+}Ti^{4+}O_3$ transforms to a $GdFeO_3$-type perovskite phase above 16 GPa, but, upon pressure release to ambient conditions, it does not turn back into the ilmenite structure, rather it transforms to a $LiNbO_3$-type structure, which also presents a corundum-like structure with diagonal cation ordering.[91,92]

Magnetic properties

To ensure reproducibility, two samples of ε-Mn_2O_3 from different batches were studied. They showed an overall similar behavior with the antiferromagnetic ordering transition around T_N = 210 K (Figure 4). Above this transition, the inverse susceptibility $1/\chi$ shows a linear

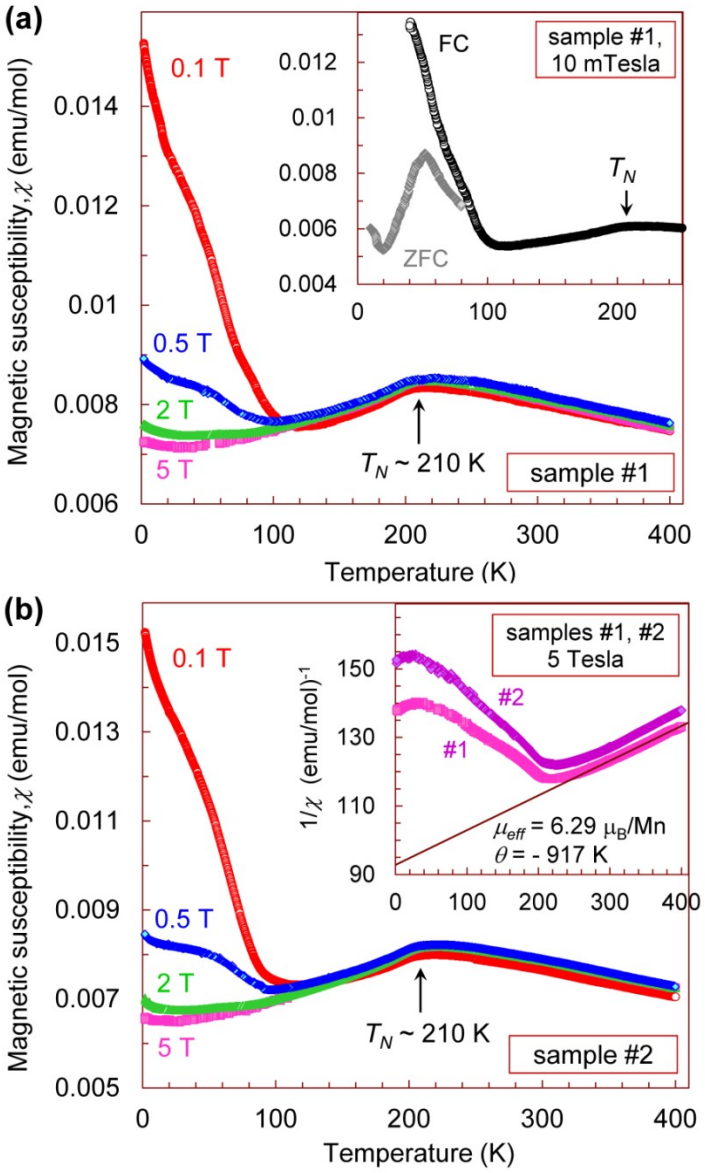

Figure 4. Temperature dependence of the magnetic susceptibility, χ of crystalline samples of ilmenite-type ε-Mn_2O_3, #1 (*a*) and #2 (*b*) at normal pressure and in different magnetic fields (labelled near the curves). Both samples demonstrate antiferromagnetic ordering below T_N ~ 210 K followed by the appearance of a minor uncompensated moment at low temperatures. The inset in (*a*) shows the difference between the field-cooling (FC) and zero-field-cooling (ZFC) magnetic susceptibilities at 10 mT field. The inset in (*b*) shows the temperature dependence of the inverse magnetic susceptibility ($1/\chi$) in a magnetic field of 5 T. An example of the Curie-Weiss fit for sample #1 is shown.

Curie-Weiss-like behavior with the effective moment of 6.29 μ_B/Mn in sample #1 and 6.02 μ_B/Mn in sample #2 (inset in Figure 4b). Both values are somewhat higher than 5.02 μ_B/Mn

expected for the mixture of Mn^{2+} and Mn^{4+} in ε-Mn_2O_3, indicating that the true paramagnetic regime was probably not reached. Measurements above 400 K were unfortunately impossible due to the proclivity of the samples for decomposition upon heating. The Curie-Weiss temperatures of -917 K and -850 K in samples #1 and #2, respectively (inset in Figure 4b), indicate the predominant antiferromagnetic interactions similar to other Mn_2O_3 polymorphs.

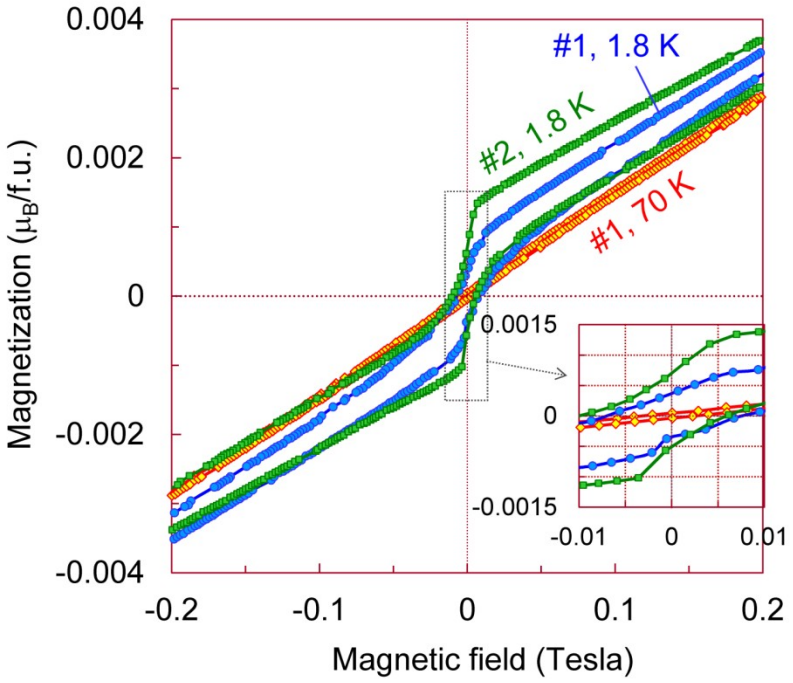

Figure 5. Magnetization isotherms for two crystalline samples of ilmenite-type ε-Mn_2O_3 (#1, #2) at two temperatures, 1.8 K and 70 K. The inset shows a magnified central area of this plot.

Below T_N, the magnetic susceptibility decreases upon cooling, as typical for long-range-ordered antiferromagnets, but below 100 K it increases again, although in low applied fields only (Figure 4). From the splitting of the field-cooled and zero-field-cooled data (inset in Figure 4a), we infer that a weak freezing effect takes place around 80 K, and a minute uncompensated moment of less than 0.002 μ_B/f.u. develops at low temperatures (Figure 5). The size of this uncompensated moment is rather similar in both samples.

Different oxidation states of Mn1 and Mn2 atoms do not allow a full compensation of the respective magnetic sublattices. Therefore, antiparallel spin alignment on Mn1 and Mn2 sites would result in a ferrimagnetic state, which is not observed experimentally. It seems likely that spins align antiferromagnetically within each of Mn1 and Mn2 sublattices, thus yielding a fully compensated antiferromagnetic state. Our DFT calculations suggest that such an antiferromagnetic state is 1.1 meV/f.u. lower in energy than the ferrimagnetic state. This elucidates the antiferromagnetic ground state of ε-Mn_2O_3 despite the charge disproportionation of the Mn atoms.

XANES spectra

To examine the electronic state of the Mn ions in ilmenite ε-Mn_2O_3 phase, we measured its XANES spectrum from a bulk polycrystalline sample (Figure 6a). This spectrum exhibited a well-defined pre-edge peak at 6541.3 eV. A comparative analysis of the pre-edge peaks in Mn-bearing oxides reported in the literature[93] suggests that the pre-edge peak at about 6541 eV corresponds to the average oxidation state of Mn^{3+}. For comparison, we acquired XANES spectra of two other Mn_2O_3 polymorphs at the same conditions, conventional α-Mn_2O_3 phase with the cubic-bixbyite-type structure that has exclusively Mn^{3+} ions,[55] and high-pressure quadruple perovskite ζ-Mn_2O_3 phase (Figure 6a), which was earlier established to contain Mn^{2+} and Mn^{4+} cations in significant amounts, in addition to the dominant group of Mn^{3+}.[56] We observed that the overall shapes of these three XANES spectra are quite similar (Figure 6a). This fact also points out that the average oxidation state of Mn^{3+} in ε-Mn_2O_3 is the same as in the two other polymorphs. Meanwhile, one can note the differences between all three spectra. In particular, the pre-edge single peak of ε-Mn_2O_3 strongly differed from the doublet features of α-Mn_2O_3 and ζ-Mn_2O_3. Furthermore, the spectra of both high-pressure

polymorphs, ε-Mn_2O_3 and ζ-Mn_2O_3 exhibited a shoulder of the absorption edge near 6551 eV, which was absent in the spectrum of α-Mn_2O_3 (Figure 6a).

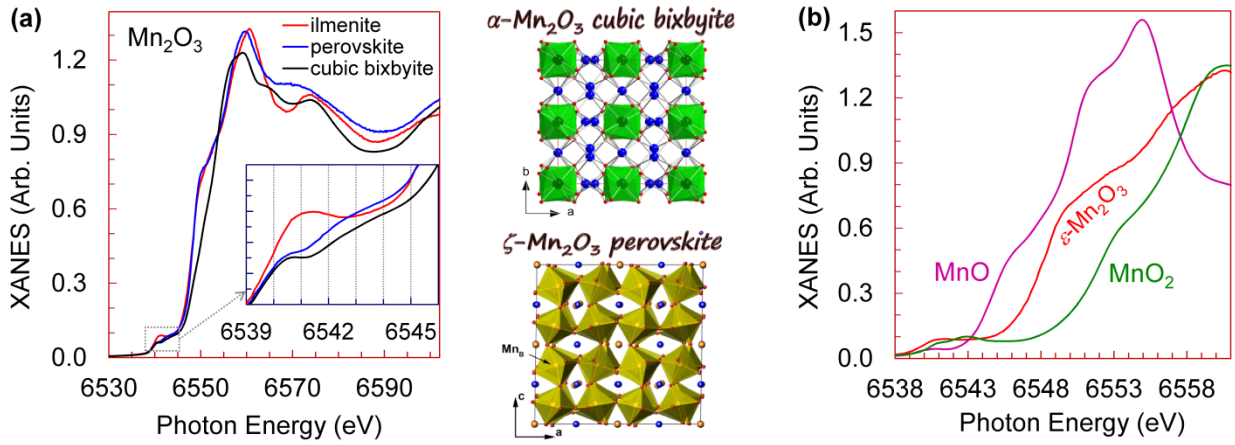

Figure 6. Normalized XANES spectra at the Mn K-edge of ilmenite-type ε-Mn_2O_3 at normal conditions. (*a*) Comparative spectra of three Mn_2O_3 phases: ilmenite-type ε-Mn_2O_3, quadruple perovskite ζ-Mn_2O_3, and cubic-bixbyite-type α-Mn_2O_3. The inset shows the magnified pre-edge features of these spectra. The crystal structures of α-Mn_2O_3 and ζ-Mn_2O_3 are shown in the middle, between plots (*a*) and (*b*). (*b*) Comparison of the absorption edges for ilmenite-type ε-Mn_2O_3 and for reference materials, MnO and β-MnO_2 obtained on the same setup. The absorption edge for ε-Mn_2O_3 lies in the middle between those of MnO and MnO_2. This confirms the average oxidation state of Mn^{3+} in ε-Mn_2O_3.

The pre-edge peak features in XANES spectra of *3d* transition-metal compounds are often ascribed to the *1s*→*3d* electronic transition in the literature.[94] However, this quadrupole transition should result in a relatively weak pre-edge doublet. Such features were reported, for example, for Co^{2+} ions in a cubic quadruple perovskite.[70] An analysis of XANES spectra of *3d* transition metals with different coordination numbers showed that high-intensive pre-edge peak should be predominantly related to *d-p* hybridization that results in an electric dipole transition,[94] rather than the much weaker *1s*→*3d* transition.[94] In accordance with this analysis, the highly-intense pre-edge peaks are expected for tetrahedrally-coordinated *3d* ions; by contrast, *3d* ions with either octahedral or square-planar coordination should not

exhibit pronounced pre-edge peaks.[94] Thus, the appearance of the distinct but rather weak pre-edge peak in the spectra of ε-Mn_2O_3 could be tentatively assigned to the very strong distortions of Mn2 octahedra that are filled with Mn^{2+} ions (Figure 1c). In contrast, both the cubic-bixbyite α-Mn_2O_3 and quadruple perovskite ζ-Mn_2O_3 structures are characterized by only moderate distortions in the cation coordination.[55,56] This fact could explain the much weaker intensities of the pre-edge features in the XANES spectra of α-Mn_2O_3 and ζ-Mn_2O_3 (inset in Figure 6a). The latter could be assigned to quadrupole *1s→3d* transitions.[94]

In Figure 6b, we compare the XANES spectra for ε-Mn_2O_3 with those of the other simple manganese oxides (MnO and β-MnO_2 pyrolusite) obtained at the same setup at ambient conditions. Note that similar spectra for MnO and β-MnO_2 pyrolusite were reported in the literature.[95-97] As seen from Figure 6b, the absorption edges of ε-Mn_2O_3 lie in the middle between the edges of MnO and β-MnO_2, consistent with the average Mn^{3+} oxidation state in this polymorph. It is interesting to note that both MnO and β-MnO_2 also demonstrated the shoulders in their absorption edges, but not as strong as those in the high-pressure phases (Figure 6b).

Electronic properties

At normal conditions, ilmenite-type ε-Mn_2O_3 was characterized by high electrical resistance values that suggested its semiconducting nature. To determine a band gap value of this polymorph, we measured absorption spectra of selected four single-crystalline double-polished samples. In the near IR region, we observed a rather abrupt increase in the absorption coefficient with energy, suggesting the existence of a distinct band gap (Figure 7). Generally, the profiles of the absorption edges in all spectra look quite ordinary, and hence,

they can be fitted well by a common model for parabolic bands. In this model, the absorption coefficient, α is determined as a function of the energy (E) as $\alpha = \alpha_0 \left[\left(E - E_g \right) / E_g \right]^n + C$,

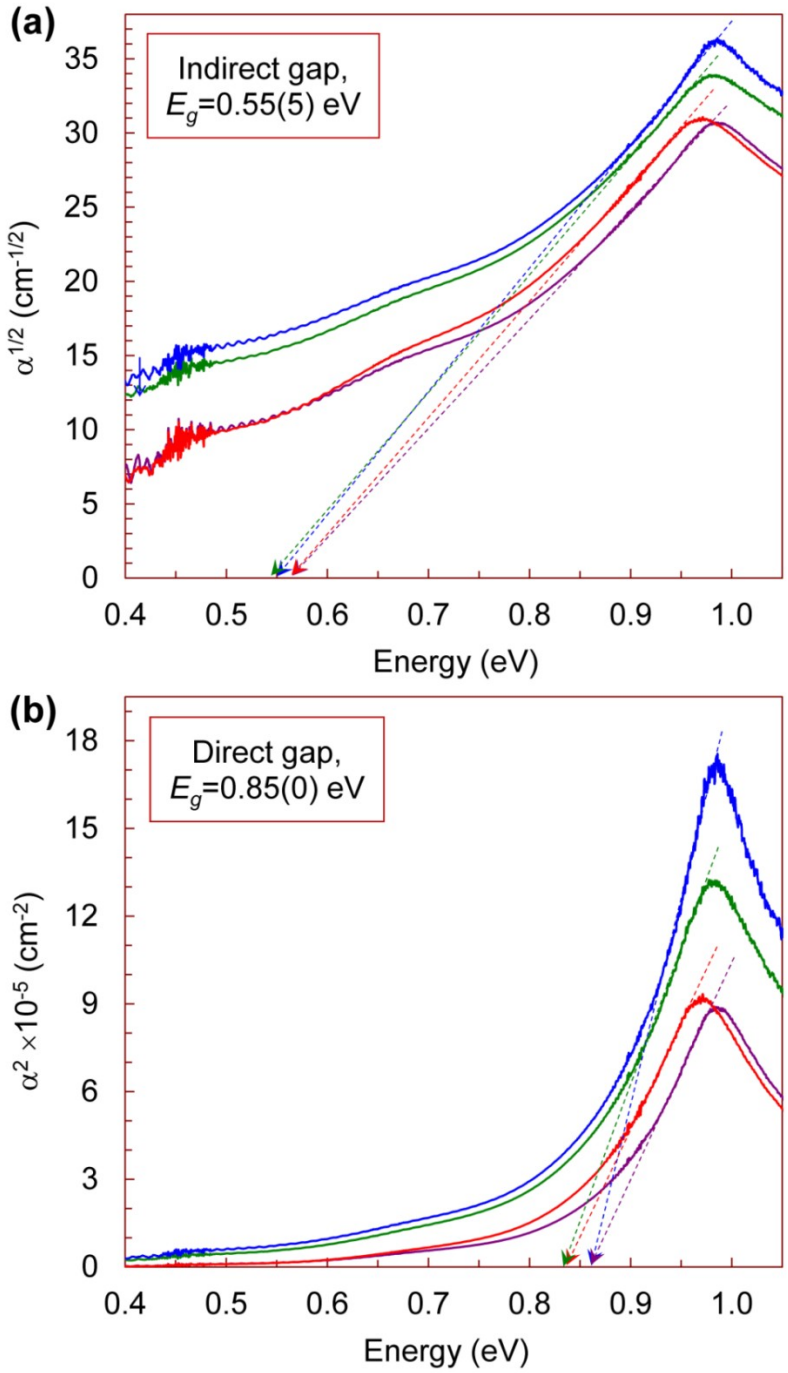

Figure 7. Near IR absorption spectra (α is the absorption coefficient) of ilmenite-type ε-Mn_2O_3 acquired at normal conditions on four different crystals (shown in different colors). The spectra are shown in two representations, as $\alpha^{1/2}$ *vs* energy (*a*) and as α^2 *vs* energy (*b*) for the determination of the indirect and direct band gaps, respectively.

where α_0 is a constant, E_g is the band gap, C is a small instrumental shift, and $n = {}^1/_2$ and $n = 2$ for direct and indirect band gaps, respectively.[61] Using this expression we established that ilmenite ε-Mn_2O_3 is an indirect-band-gap semiconductor with a fundamental gap of E_g = 0.55(5) eV (Figure 7a). A minimal direct band gap in this phase was found to be E_g = 0.85 eV (Figure 7b). DFT calculations returned a somewhat larger band gap of 1.8 eV (Figure 8), but this value is strongly dependent on the DFT+U parameters. It is also worth noting that optical band gaps of other Mn oxides strongly depend on the sample morphology. For example, the band gap of α-Mn_2O_3 is reported as E_g=1.25 eV[98-100] or E_g=3.3 eV.[15,101] Meanwhile, a band gap in the higher-pressure polymorph, – perovskite-type ξ-Mn_2O_3 was reported to be E_g = 0.45 eV,[61] i.e., even slightly smaller than the band gap in ε-Mn_2O_3 (Figure 7).

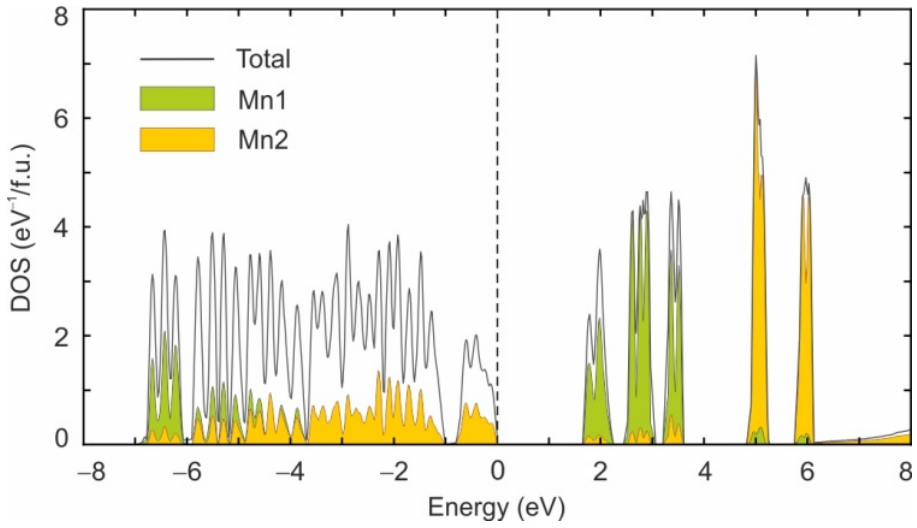

Figure 8. Total and atomic-resolved density of states calculated for the lowest-energy antiferromagnetic spin configuration of ilmenite-type ε-Mn_2O_3. The Fermi level is at zero energy. The larger number of unoccupied states for Mn1 compared to Mn2 illustrates the +4 oxidation state of the former and the +2 oxidation state of the latter.

To probe the high-pressure response of the electronic state of ilmenite-type ε-Mn_2O_3, we measured electrical resistance as a function of applied pressure up to 9.5 GPa on one of the crystals (Figure 9). We observed that the semiconducting properties of ε-Mn_2O_3 are preserved in this pressure range, suggesting the structural and electronic stability of the compound. The

pressure behavior of the electrical resistance of ε-Mn_2O_3 differed from those of cubic-bixbyite α-Mn_2O_3[58] and perovskite-type ζ-Mn_2O_3,[61] which both demonstrated a multi-order pressure-driven enhancement of electrical conductivity. Thus, the electronic state in ε-Mn_2O_3 polymorph with the mixed +2 and +4 valences seems to be more robust to applied stresses than those in trivalent cubic-bixbyite α-Mn_2O_3 or predominantly (~70%) three-valence perovskite-type ζ-Mn_2O_3. At normal pressure, the electrical resistance of ilmenite-type ε-Mn_2O_3 was too high to reliably measure its Seebeck coefficient

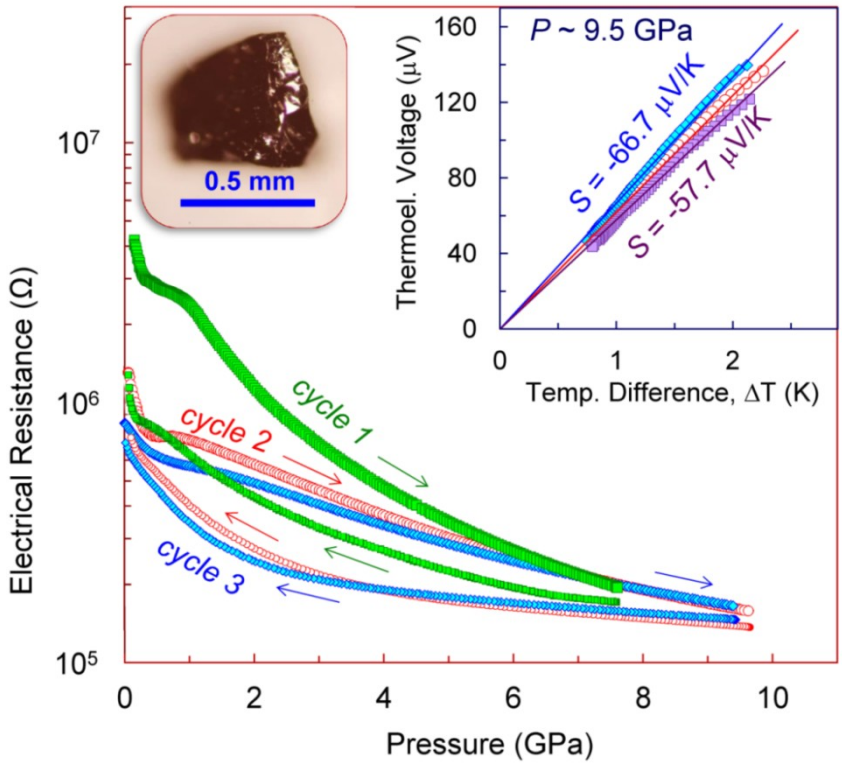

Figure 9. Pressure dependence of electrical resistance of ilmenite-type ε-Mn_2O_3 for three subsequent pressure cycles at 295 K. Photograph of typical brown-colored crystal of ε-Mn_2O_3 is shown in the plot. The inset shows the determination of thermopower value (S) from linear slopes of thermoelectric signal (ΔU) on temperature difference (ΔT) as $S=-\Delta U/\Delta T$ at the maximum pressure of about 9.5 GPa in different pressure cycles (given by different colors).

(thermoelectric power). But it decreased a bit under pressure, and at the maximum pressure of ~9.5 GPa we could determine a Seebeck coefficient of about $S\approx$-60 μV/K (inset in Figure 9).

The negative sign of this coefficient indicated the dominant *n*-type electrical conductivity in ε-Mn_2O_3. Earlier, it was established that perovskite-type ζ-Mn_2O_3 has, on the contrary, the dominant *p*-type conductivity at normal and moderately high pressures.[61]

IV. CONCLUSIONS

In summary, we synthesized single crystals of ε-Mn_2O_3 polymorph, determined its crystal structure, and investigated magnetic and electronic properties. We established that ε-Mn_2O_3 adopts the ilmenite-type structure, which is structurally similar to corundum, but comprises two different octahedrally-coordinated positions filled with differently-charged cations, i.e., $Mn^{2+}Mn^{4+}O_3$. We experimentally determined that ε-Mn_2O_3 is a narrow-band-gap semiconductor with an indirect band gap of E_g=0.55 eV and the dominant *n*-type electrical conductivity. Magnetic susceptibility measurements revealed an antiferromagnetic order below T_N~210 K. Ilmenite-type ε-Mn_2O_3 can be promising for the semiconductor industry and could be utilized in other applications, e.g., for catalysis.

FIGURES

Figure 1. (*a*, *b*) Crystal structure of ilmenite-type ε-Mn_2O_3 at ambient conditions in two different projections. (*c*) The oxygen octahedra of Mn1 and Mn2 atoms.

Figure 2. Dependence of volumes of coordination octahedra on oxidation state for Mn ions at ambient conditions, determined for manganese oxides with well-known oxidation states of cations, e.g., for oxides containing Na^+, Li^+, Ca^{2+}, Mg^{2+}, La^{3+}, and Ti^{4+} cations. We considered high-quality data from FIZ Karlsruhe database (https://www.ccdc.cam.ac.uk/structures/). Our data for Mn1 and Mn2 octahedra in the structure of ilmenite-type ε-Mn_2O_3 are shown by red symbols. The solid line serves as a guide to the eye.

Figure 3. Pressure-temperature phase diagram of Mn_2O_3 established by HP-HT synthesis experiments. The boundaries between ilmenite-type ε-Mn_2O_3, cubic-bixbyite-type α-Mn_2O_3, and perovskite-type ζ-Mn_2O_3 phases depend on pressure-temperature conditions only. The high-temperature boundary between Mn_2O_3 and Mn_3O_4 is very sensitive to the oxygen fugacity conditions during HP-HT synthesis. Above 22-23 GPa at high temperatures, Mn_2O_3 was found to undergo a further phase transitions. These high-pressure phases were unquenchable to ambient conditions, and the recovered samples were crumbling powders with ilmenite-like structures. According to the literature, several phases can appear in the high pressure region, namely, perovskite-type η-Mn_2O_3,[57,51] post-perovskite-type δ-Mn_2O_3,[60] and orthorhombically-distorted θ-Mn_2O_3 phase.[58,59] Room-temperature studies documented a monoclinic distortion in the structure above 18 GPa.[89]

Figure 4. Temperature dependence of the magnetic susceptibility, χ of crystalline samples of ilmenite-type ε-Mn_2O_3, #1 (*a*) and #2 (*b*) at normal pressure and in different magnetic fields (labelled near the curves). Both samples demonstrate antiferromagnetic ordering below T_N ~ 210 K followed by the appearance of a minor uncompensated moment at low temperatures.

The inset in (*a*) shows the difference between the field-cooling (FC) and zero-field-cooling (ZFC) magnetic susceptibilities at 10 mT field. The inset in (*b*) shows the temperature dependence of the inverse magnetic susceptibility ($1/\chi$) in a magnetic field of 5 T. An example of the Curie-Weiss fit for sample #1 is shown.

Figure 5. Magnetization isotherms for two crystalline samples of ilmenite-type ε-Mn_2O_3 (#1, #2) at two temperatures, 1.8 K and 70 K. The inset shows a magnified central area of this plot.

Figure 6. Normalized XANES spectra at the Mn K-edge of ilmenite-type ε-Mn_2O_3 at normal conditions. (*a*) Comparative spectra of three Mn_2O_3 phases: ilmenite-type ε-Mn_2O_3, quadruple perovskite ζ-Mn_2O_3, and cubic-bixbyite-type α-Mn_2O_3. The inset shows the magnified pre-edge features of these spectra. The crystal structures of α-Mn_2O_3 and ζ-Mn_2O_3 are shown in the middle, between plots (*a*) and (*b*). (*b*) Comparison of the absorption edges for ilmenite-type ε-Mn_2O_3 and for reference materials, MnO and β-MnO_2 obtained on the same setup. The absorption edge for ε-Mn_2O_3 lies in the middle between those of MnO and MnO_2. This confirms the average oxidation state of Mn^{3+} in ε-Mn_2O_3.

Figure 7. Near IR absorption spectra (α is the absorption coefficient) of ilmenite-type ε-Mn_2O_3 acquired at normal conditions on four different crystals (shown in different colors). The spectra are shown in two representations, as $\alpha^{1/2}$ *vs* energy (*a*) and as α^2 *vs* energy (*b*) for the determination of the indirect and direct band gaps, respectively.

Figure 8. Total and atomic-resolved density of states calculated for the lowest-energy antiferromagnetic spin configuration of ilmenite-type ε-Mn_2O_3. The Fermi level is at zero energy. The larger number of unoccupied states for Mn1 compared to Mn2 illustrates the +4 oxidation state of the former and the +2 oxidation state of the latter.

Figure 9. Pressure dependence of electrical resistance of ilmenite-type ε-Mn_2O_3 for three subsequent pressure cycles at 295 K. Photograph of typical brown-colored crystal of ε-Mn_2O_3 is shown in the plot. The inset shows the determination of thermopower value (S) from linear slopes of thermoelectric signal (ΔU) on temperature difference (ΔT) as $S=-\Delta U/\Delta T$ at the maximum pressure of about 9.5 GPa in different pressure cycles (given by different colors).

Table 1. Parameters of the crystal structure of the ilmenite-type ε-Mn_2O_3 and its refinement from single-crystal X-ray diffraction at ambient conditions.

Phase:	ilmenite-type ε-Mn_2O_3
Details of the crystal structure:	
Pressure (GPa)	0
Temperature (K)	293
Crystal system,	Trigonal
Space group (No.)	$R\bar{3}$ (No. 148)
Lattice parameter, a (Å)	5.0148(8)
Lattice parameter, c (Å)	14.1141(28)
Unit cell volume, V (Å^3)	307.39(11)
Z	6
Calculated density (g/cm^3)	5.1188
Details of the crystal structure refinement:	
R_{int}, wR_2	0.0658, 0.0755
Goodness of fit	4.97
Number of reflections	317
Number of parameters	16
The Mn-O distances in the octahedra:	
Mn1–O, Å	1.9019 (×3)
Mn1–O, Å	1.9338 (×3)
Mn2–O, Å	2.0425 (×3)
Mn2–O, Å	2.2991 (×3)

Atomic coordinates:

Atom	Site	x/a	y/b	z/c
Mn1	6c	2/3	1/3	0.67408(9)
Mn2	6a	1/3	2/3	0.52976(10)
O	18f	0.6955(8)	0.6538(8	0.5912(3)

)

Anisotropic displacement parameters, in $Å^2$

Atom	U_{11}	U_{22}	U_{33}
Mn1	0.0111(4)	0.0111(4)	0.0121(6)
Mn2	0.0120(4)	0.0120(4)	0.0157(7)
O	0.0169(15)	0.0129(14)	0.0165(16)

ASSOCIATED CONTENT

Crystallographic Information File for the ilmenite-type Mn_2O_3 (CIF).

AUTHOR INFORMATION

Corresponding Author

Sergey V. Ovsyannikov
Bayerisches Geoinstitut
Universität Bayreuth
Universitätsstrasse 30
D-95447 Bayreuth
Germany;
https://orcid.org/0000-0003-1027-0998;
E-mail: Sergey.Ovsyannikov@uni-bayreuth.de

Notes

The authors declare no competing financial interest.

ACKNOWLEDGMENTS

The authors thank Raphael Njul for polishing of the samples and Prof. Hans Keppler (BGI) for assistance in the IR absorption studies. The work was partly supported by the Deutsche Forschungsgemeinschaft (DFG, German Research Foundation) – Grant No. OV-110/3-2. The electrical resistance and thermopower measurements were carried out within the framework of the state assignment of Ministry of Science and Higher Education of the Russian Federation (theme “Electron” No. AAAA-A18-118020190098-5).

ABBREVIATIONS

HP-HT, high-pressure high-temperature; XANES, X-ray absorption near edge spectra

REFERENCES

(1). Seo, W. S.; Jo, H. H.; Lee, K.; Kim, B.; Oh, S. J.; Park, J. T. Size-Dependent Magnetic Properties of Colloidal Mn_3O_4 and MnO Nanoparticles. *Angew. Chem. Int. Ed.* **2004**, *43*, 1115–1115.

(2). Kim, S. H.; Choi, B. J.; Lee, G. H.; Oh, S. J.; Kim, B.; Choi, H. C.; Park, J.; Chang, Y. Ferrimagnetism in γ-Manganese Sesquioxide (γ−Mn_2O_3) Nanoparticles. *J. Korean Phys. Soc.* **2005**, *46*, 941-944.

(3). Regulski, M.; Przeniosło, R.; Sosnowska, I.; Hohlwein, D.; Schneider, R. Neutron Diffraction Study of the Magnetic Structure of α-Mn_2O_3. *J. All. Comp.* **2004**, *362*, 236–240.

(4). Chandra, M.; Yadav, S.; Choudhary, R. J.; Rawat, R.; Sinha, A. K.; Lepetit, M.-B.; Singh, K. Multiferroicity and Magnetoelastic Coupling in $\alpha-Mn_2O_3$: A Binary Perovskite. *Phys. Rev. B* **2020**, *98*, 104427.

(5). Chandra, M.; Yadav, S.; Rawat, R.; Singh, K. Enhancement of Magnetoelectric Coupling in Cr doped Mn_2O_3. *J. Phys.: Condens. Matter* **2020**, *32*, 295703.

(6). Abrashev, M. V.; Chernev, P.; Kubella, P.; Mohammadi, M. R.; Pasquini, C.; Dau, H.; Zaharieva, I. Origin of the Heat-Induced Improvement of Catalytic Activity and Stability of MnO_x Electrocatalysts for Water Oxidation. *J. Mater. Chem. A*, **2019**, ***7***, 17022-17036.

(7). Han, Y.-F.; Ramesh, K.; Chen, L.; Widjaja, E.; Chilukoti, S.; Chen, F. Observation of the Reversible Phase-Transformation of α-Mn_2O_3 Nanocrystals during the Catalytic Combustion of Methane by *in-Situ* Raman Spectroscopy. *J. Phys. Chem. C* **2007**, *111*, 2830–2833.

(8). Lacerda, J. N.; Franceschini, D. F.; Ponzio, E. A.; Esteves, L. M.; Guimaraes, R. B.; Xing, Y. T. Manganese Oxide Nanofoam Prepared by Pulsed Laser Deposition for High Performance Supercapacitor Electrodes. *Mater. Chem. Phys.* **2020**, *242*, 122459.

(9). Becker, D.; Klos, M.; Kickelbick, G. Mechanochemical Synthesis of Mn_3O_4 Nanocrystals and Their Lithium Intercalation Capability. *Inorg. Chem.* **2019**, *58*, 15021-15024.

(10). Lin, X.; Lin, J.; Deng, H.; Krishna Reddy, R. C.; Liu, J. Structural Diversity of Zinc(II), Manganese(II), and Gadolinium(III) Coordination Polymers Based on Two Isomeric N-Heteroaromatic Polycarboxylate Ligands: Structures and Their Derived Mn_2O_3 for Lithium Storage Applications. *Inorg. Chem.* **2020**, *59*, 460–471.

(11). Hertzberg, B. J.; Huang, A.; Hsieh, A.; Chamoun, M.; Davies, G.; Seo, J. K.; Zhong, Z.; Croft, M.; Erdonmez, C.; Meng, Y. S.; Steingart, D. Effect of Multiple Cation Electrolyte Mixtures on Rechargeable Zn–MnO_2 Alkaline Battery. *Chem. Mater.* **2016**, *28*, 4536–4545.

(12). Abdullah, M. M.; Siddiqui, S. A.; Al-Abbas, S. M. Physio-Chemical Properties and Dielectric Behavior of As-Grown Manganese Oxide (γ-Mn_2O_3) Nanoparticles. *J. Electron. Mater.* **2020**, *49*, 4410–4417.

(13). Gupta, P. K.; Bhandari, A.; Saha, S.; Bhattacharya, J.; Pala, R. G. S. Modulating Oxygen Evolution Reactivity in MnO_2 through Polymorphic Engineering. *J. Phys. Chem. C* **2019**, *123*, 22345–22357.

(14). Du, L.; Yu, S.; Liu, X.; Ding, Y. An Efficient Atomic Layer Deposition Process of MnO_x Films Using bis(N,N′-di-tert-butylacetamidinato)manganese-(II) and H_2O as Reactants. *Appl. Surf. Sci.* **2019**, *486*, 460-465.

(15). Pal, N.; Sharma, A.; Acharya, V.; Chourasia, N. K.; Biring, S.; Pal, B. N. Gate Interface Engineering for Subvolt Metal Oxide Transistor Fabrication by Using Ion-Conducting Dielectric with Mn_2O_3 Gate Interface. *ACS Appl. Electron. Mater.* **2020**, *2*, 25−34.

(16). Chatterji**,** T. (Ed.), *Colossal Magnetoresistive Manganites* (Kluwer Academic Publishers, Dordrechti Boston *I* London, 2004).

(17). Prodi, A.; Gilioli, E.; Gauzzi, A.; Licci, F.; Marezio, M.; Bolzoni, F.; Huang, Q.; Santoro, A.; Lynn, J. W. Charge, Orbital and Spin Ordering Phenomena in the Mixed Valence Manganite ($NaMn_3^{3+}$)($Mn_2^{3+}Mn_2^{4+}$)O_{12}. *Nat. Mater.* **2004**, *3*, 48-52.

(18). Glazkova, Y. S.; Terada, N.; Matsushita, Y.; Katsuya, Y.; Tanaka, M.; Sobolev, A. V.; Presniakov, I. A.; Belik, A. A. High-Pressure Synthesis, Crystal Structures, and Properties of $CdMn_7O_{12}$ and $SrMn_7O_{12}$ Perovskites. *Inorg. Chem.* **2015**, *54*, 9081–9091.

(19). Belik, A. A.; Glazkova, Y. S.; Katsuya, Y.; Tanaka, M.; Sobolev, A. V.; Presniakov, I. A. Low-Temperature Structural Modulations in $CdMn_7O_{12}$, $CaMn_7O_{12}$, $SrMn_7O_{12}$, and $PbMn_7O_{12}$ Perovskites Studied by Synchrotron X-ray Powder Diffraction and Mössbauer Spectroscopy. *J. Phys. Chem. C* **2016**, *120*, 8278–8288.

(20). Belik, A. A.; Glazkova, Y. S.; Terada, N.; Matsushita, Y.; Sobolev, A. V.; Presniakov, I. A.; Tsujii, N.; Nimori, S.; Takehana, K.; Imanaka, Y. Spin-Driven Multiferroic Properties of $PbMn_7O_{12}$ Perovskite. *Inorg. Chem.* **2016**, *55*, 6169–6177.

(21). Belik, A. A.; Matsushita, Y.; Khalyavin, D. D. Reentrant Structural Transitions and Collapse of Charge and Orbital Orders in Quadruple Perovskites. *Angew. Chem. Intl. Ed.* **2017**, *56*, 10423-10427.

(22). Johnson, R. D.; Khalyavin, D. D.; Manuel, P.; Radaelli, P. G.; Glazkova, I. S.; Terada, N.; Belik, A. A. Magneto-Orbital Ordering in the Divalent A-site Quadruple Perovskite Manganites $A Mn_7O_{12}$ (A=Sr, Cd, and Pb). *Phys. Rev. B* **2017**, *96*, 054448.

(23). Johnson, R. D.; Khalyavin, D. D.; Manuel, P.; Zhang, L.; Yamaura, K.; Belik, A. A. Magnetic Structures of the Rare-Earth Quadruple Perovskite Manganites $R Mn_7O_{12}$. *Phys. Rev. B* **2018**, *98*, 104423.

(24). Verseils, M.; Mezzadri, F.; Delmonte, D.; Cabassi, R.; Baptiste, B.; Klein, Y.; Calestani, G.; Bolzoni, F.; Gilioli, E.; Gauzzi, A. Centrosymmetry Breaking and

Ferroelectricity Driven by Short-Range Magnetic Order in the Quadruple Perovskite $(YMn_3)Mn_4O_{12}$. *Inorg. Chem.* **2019**, *58*, 14204-14211.

(25). Gauzzi, A.; Milton, F. P.; Pascotto Gastaldo, V.; Verseils, M.; Gualdi, A. J.; von Dreifus, D.; Klein, Y.; Garcia, D.; de Oliveira, A. J. A.; Bordet, P.; Gilioli, E. Ferroelectricity in the 1 μC cm^{-2} Range Induced by Canted Antiferromagnetism in $(LaMn_3)Mn_4O_{12}$. *Appl. Phys. Lett.* **2019**, *115*, 152902.

(26). Gautam, K.; Majid, S. S.; Francoual, S.; Ahad, A.; Dey, K.; Rahn, M. C.; Sankar, R.; Chou, F. C.; Shukla, D. K. Magnetic and Orbital Correlations in Multiferroic $CaMn_7O_{12}$ Probed by X-ray Resonant Elastic Scattering. *Phys. Rev. B* **2020**, *101*, 224430.

(27). Khalyavin, D. D.; Johnson, R. D.; Orlandi, F.; Radaelli, P. G.; Manuel, P.; Belik, A. A.; Emergent Helical Texture of Electric Dipoles. *Science* **2020**, *369*, 680–684.

(28). Arévalo-López, A. M.; McNally, G. M.; Attfield, J. P. Large Magnetization and Frustration Switching of Magnetoresistance in the Double-Perovskite Ferrimagnet Mn_2FeReO_6. *Angew. Chem. Intl. Ed.* **2015**, *54*, 12074-12077.

(29). Dos santos-García, A. J.; Solana-Madruga, E.; Ritter, C.; Ávila-Brande, D.; Fabelo, O.; Sáez-Puche, R. Synthesis, Structures and Magnetic Properties of the Dimorphic Mn_2CrSbO_6 Oxide. *Dalton Trans.* **2015**, ***44***, 10665-10672.

(30). Li, M.-R.; Retuerto, M.; Deng, Z.; Stephens, P. W.; Croft, M.; Huang, Q.; Wu, H.; Deng, X.; Kotliar, G.; Sánchez-Benítez, J.; Hadermann, J.; Walker, D.; Greenblatt, M. Giant Magnetoresistance in the Half-Metallic Double-Perovskite Ferrimagnet Mn_2FeReO_6. *Angew. Chem. Intl. Ed.* **2015**, *54*, 12069-12073.

(31). Liu, L.; Song, H. X.; Li, X.; Zhang, D.; Mathieu, R.; Ivanov, S.; Skogby, H.; Lazor, P. Pressure-Induced Polymorphism and Piezochromism in Mn_2FeSbO_6. *Appl. Phys. Lett.* **2019**, *114*, 162903.

(32). Zhang, L.; Donni, A.; Pomjakushin, V. Y.; Yamaura, K.; Belik, A. A. Crystal and Magnetic Structures and Properties of $(Lu_{1-x}Mn_x)MnO_3$ Solid Solutions. *Inorg. Chem.* **2018**, *57*, 14073-14085.

(33). Li, M.-R.; Hodges, J. P.; Retuerto, M.; Deng, Z.; Stephens, P. W.; Croft, M. C.; Deng, X.; Kotliar, G.; Sánchez-Benítez, J.; Walker, D.; Greenblatt, M. Mn_2MnReO_6: Synthesis and Magnetic Structure Determination of a New Transition-Metal-Only Double Perovskite Canted Antiferromagnet. *Chem. Mater.* **2016**, *28*, 3148–3158.

(34). Li, M.-R.; Stephens, P. W.; Croft, M.; Deng, Z.; Li, W.; Jin, C.; Retuerto, M.; Hodges, J. P.; Frank, C. E.; Wu, M. X.; Walker, D.; Greenblatt, M. $Mn_2(Fe_{0.8}Mo_{0.2})MoO_6$: A Double Perovskite with Multiple Transition Metal Sublattice Magnetic Effects. *Chem. Mater.* **2018**, *30*, 4508–4514.

(35). Belik, A. A.; Matsushita, Y.; Tanaka, M.; Takayama-Muromachi, E. $(In_{1-y}Mn_y)MnO_3$ ($1/9 <= y <= 1/3$): Unusual Perovskites with Unusual Properties. *Angew. Chem. Intl. Ed.* **2010**, *49*, 7723-7727.

(36). Zhang, L.; Matsushita, Y.; Yamaura, K.; Belik, A. A. Five-Fold Ordering in High-Pressure Perovskites RMn_3O_6 (R = Gd–Tm and Y). *Inorg. Chem.* **2017**, *56*, 5210–5218.

(37). Lavina, B.; Dera, P.; Kim, E.; Meng, Y.; Downs, R. T.; Weckf, P. F.; Sutton, S. R.; Zhao, Y. Discovery of the Recoverable High-Pressure Iron Oxide Fe_4O_5. *Proc Nat. Acad. Sci. USA* **2011**, *108*, 17281–17285.

(38). Lavina, B.; Meng, Y. Unraveling the Complexity of Iron Oxides at High Pressure and Temperature: Synthesis of Fe_5O_6. *Sci. Adv.* **2015**, *1*, e1400260.

(39). Merlini, M.; Hanfland, M.; Salamat, A.; Petitgirard, S.; Müller, H. The Crystal Structures of $Mg_2Fe_2C_4O_{13}$, with Tetrahedrally Coordinated Carbon, and $Fe_{13}O_{19}$, Synthesized at Deep Mantle Conditions. *Amer. Mineral.* ***2015****, 100, 2001–2004.*

(40). Sinmyo, R.; Bykova, E.; Ovsyannikov, S. V.; McCammon, C.; Kupenko, I.; Ismailova, L.; Dubrovinsky. L. Discovery of Fe_7O_9: A New Iron Oxide with a Complex Monoclinic Structure. *Sci. Rep.* **2016**, *6*, 32852.

(41). Ishii, T.; Uenver-Thiele, L.; Woodland, A. B.; Alig, E.; Boffa Ballaran, T. Synthesis and Crystal Structure of Mg-bearing Fe_9O_{11}: New Insight in the Complexity of Fe-Mg Oxides at Conditions of the Deep Upper Mantle. *Amer. Minerol.* **2018**, *103*, 1873–1876.

(42). Bykova, E.; Dubrovinsky, L.; Dubrovinskaia, N.; Bykov, M.; McCammon, C.; Ovsyannikov, S. V.; Liermann, H.-P.; Kupenko, I.; Chumakov, A.; Rüffer, R.; Hanfland, M.; Prakapenka. V. Structural Complexity of Simple Fe_2O_3 Oxide at High Pressures and Temperatures. *Nat. Commun.* **2016**, *7*, 10661.

(43). Ovsyannikov, S. V.; Bykov, M.; Bykova, E.; Kozlenko, D. P.; Tsirlin, A. A.; Karkin, A. E.; Shchennikov, V. V.; Kichanov, S. E.; Gou, H.; Abakumov, A. M.; Egoavil, R.; Verbeeck, J.; McCammon, C.; Dyadkin, V.; Chernyshov, D.; van Smaalen, S.; Dubrovinsky, L. S. Charge Ordering Transition in Iron Oxide Fe_4O_5 Involving Competing Dimer and Trimer Formation. *Nat. Chem.* **2016**, *8*, 501-508.

(44). Ovsyannikov, S. V.; Bykov, M.; Bykova, E.; Glazyrin, K.; Manna, R. S.; Tsirlin, A. A. Cerantola, V.; Kupenko, I.; Kurnosov, A. V.; Kantor, I.; Pakhomova, A. S.;

Chuvashova, I.; Chumakov, A.; Rüffer, R.; McCammon, C.; Dubrovinsky. L. S. Pressure Tuning of Charge Ordering in Iron Oxide. *Nat. Commun.* **2018**, *9*, 4142.

(45). Ovsyannikov, S. V.; Bykov, M.; Medvedev, S. A.; Naumov, P. G.; Jesche, A.; Tsirlin, A. A.; Bykova, E.; Chuvashova, I.; Karkin, A. A.; McCammon, C.; Dyadkin, V.; Chernyshov, D.; Dubrovinsky, L. S. A Room-Temperature Verwey-Type Transition in Iron Oxide. Fe_5O_6. *Angew. Chem. Intl. Ed.* **2020**, *59*, 5632–5636.

(46). Verwey, E. J. W. Electronic Conduction of Magnetite (Fe_3O_4) and its Transition Point at Low Temperatures. *Nature* **1939**, *144*, 327-328.

(47). Senn, M. S.; Wright, J. P.; Attfield, J. P. Charge Order and Three-Site Distortions in the Verwey Structure of Magnetite. *Nature* **2012**, *481*, 173–176.

(48). Jeong, D.; Jin, K.; Jerng, S. E.; Seo, H.; Kim, D.; Nahm, S. H.; Kim, S. H.; Nam, K. T. Mn_5O_8 Nanoparticles as Efficient Water Oxidation Catalysts at Neutral pH. *ACS Catal.* **2015**, *5*, 4624−4628.

(49). Young, M. J.; Hare, C. D.; Cavanagh, A. S.; Musgrave, C. B.; George, S. M. Rapid Growth of Crystalline Mn_5O_8 by Self-Limited Multilayer Deposition using $Mn(EtCp)_2$ and O_3. *ACS Appl. Mater. Interf.* **2016**, *8*, 18560–18569.

(50). Shan, X.; Charles, D. S.; Lei, Y.; Qiao, R.; Wang, G.; Yang, W.; Feygenson, M.; Su, D.; Teng, X. Bivalence Mn_5O_8 with Hydroxylated Interphase for High-Voltage Aqueous Sodium-Ion Storage. *Nat. Commun.* **2016**, *7*, 13370.

(51). Chariton, S. The elastic properties and the crystal chemistry of carbonates in the deep Earth (Doctoral thesis, 2019, University of Bayreuth) https://doi.org/10.15495/EPub_UBT_00004592

(52). Ross II, A. R.; Rubie, D. C.; Paris, E. Rietveld Refinement of the High-Pressure Polymorph of Mn_3O_4, *Amer. Mineral.* **1990**, *75*, 1249-1252.

(53). Lv, H.; Yao, M.; Li, Q.; Li, Z.; Liu, B.; Liu, R.; Lu, S.; Li, D.; Mao, J.; Ji, X.; Liu, J.; Chen, Z.; Zou, B.; Cui, T.; Liu, B. B. Effect of Grain Size on Pressure-Induced Structural Transition in Mn_3O_4, *J. Phys. Chem. C* **2012**, *116*, 2165–2171.

(54). Darul, J.; Lathe, C.; Piszora, P. Mn_3O_4 under High Pressure and Temperature: Thermal Stability, Polymorphism, and Elastic Properties. *J. Phys. Chem. C* **2013**, *117*, 23487−23494.

(55). Geller, S. Structures of alfa-Mn_2O_3, $(Mn_{0.983}Fe_{0.017})_2O_3$ and $(Mn_{0.37}Fe_{0.63})_2O_3$ and Relation to Magnetic Ordering. *Acta Cryst.* **1971**, *B27*, 821-828.

(56). Ovsyannikov, S. V.; Abakumov, A. M.; Tsirlin, A. A.; Schnelle, W.; Egoavil, R.; Verbeeck, J.; Van Tendeloo, G.; Glazyrin, K.; Hanfland, M.; Dubrovinsky, L. Perovskite-like Mn_2O_3: A Path to New Manganites. *Angew. Chem. Intl. Ed.* **2013**, *52*, 1494-1498.

(57). Boulard, E.; Liu, Y.; Koh, A. L.; Reagan, M. M.; Stodolna, J.; Morard, G.; Mezouar, M.; Mao, W. L. Transformations and Decomposition of $MnCO_3$ at Earth's Lower Mantle Conditions. *Front. Earth Sci.* **2016**, *4*, 107.

(58). Hong, F.; Yue, B.; Hirao, N.; Liu, Z.; Chen, B. Significant Improvement in Mn_2O_3 Transition Metal Oxide Electrical Conductivity via High Pressure. *Sci. Rep.* **2017**, *7*, 44078.

(59). Yue, B.; Hong, F.; Hirao, N.; Vasin, R.; Wenk, H.-R.; Chen, B.; Mao, H.-K. A Simple Variant Selection in Stress-Driven Martensitic Transformation. *Proc. Nat. Sci. Acd. USA* **2019**, *116*, 14905–14909.

(60). Santillan, J.; Shim, S.-H.; Shen, G.; Prakapenka, V. B. High-Pressure Phase Transition in Mn_2O_3: Application for the Crystal Structure and Preferred Orientation of the $CaIrO_3$ Type. *Geophys. Res. Lett.* **2006**, *33*, L15307.

(61). Ovsyannikov, S. V.; Karkin, A. E.; Morozova, N. V.; Shchennikov, V. V.; Bykova, E.; Abakumov, A. M.; Tsirlin, A. A.; Glazyrin, K. V.; Dubrovinsky, L. A Hard Oxide Semiconductor with a Direct and Narrow Bandgap and Switchable *p-n* Electrical Conduction. *Adv. Mater.* **2014**, *26*, 8185–8191.

(62). Cong, J.; Zhai, K.; Chai, Y.; Shang, D.; Khalyavin, D. D.; Johnson, R. D.; Kozlenko, D. P.; Kichanov, S. E.; Abakumov, A. M.; Tsirlin, A. A.; Dubrovinsky, L.; Xu, X.; Sheng, Z.; Ovsyannikov, S. V.; Sun, Y. Spin-Induced Multiferroicity in the Binary Perovskite Manganite Mn_2O_3. *Nat. Commun.* **2018**, *9*, 2996.

(63). Khalyavin, D. D.; Johnson, R. D.; Manuel, P.; Tsirlin, A. A.; Abakumov, A. M.; Kozlenko, D. P.; Sun, Y.; Dubrovinsky, L.; Ovsyannikov, S. V. Magneto-Orbital Texture in the Perovskite Modification of Mn_2O_3. *Phys. Rev. B* **2018**, *98*, 014426.

(64). Manjón, F. J.; Sans, J. A.; Ibáñez, J.; Pereira, A. L. J. Pressure-Induced Phase Transitions in Sesquioxides. *Crystals* **2019**, *9*, 630.

(65). Köksal, O.; Baidya, S.; Pentcheva, R. Confinement-Driven Electronic and Topological Phases in Corundum-Derived *3d*-Oxide Honeycomb Lattices. *Phys. Rev. B* **2018**, *97*, 035126.

(66). Ibáñez, J.; Sans, J. Á.; Cuenca-Gotor, V.; Oliva, R.; Gomis, Ó.; Rodríguez-Hernández, P.; Muñoz, A.; Rodríguez-Mendoza, U.; Velázquez, M.; Veber, P.; Popescu, C.; Manjón, F. J. Structural and Lattice-Dynamical Properties of Tb_2O_3 under

Compression: A Comparative Study with Rare Earth and Related Sesquioxides. *Inorg. Chem.* **2020**, 59, 9648–9666

(67). Belik, A. A.; Furubayashi, T.; Yusa, H.; Takayama-Muromachi, E. Perovskite, $LiNbO_3$, Corundum, and Hexagonal Polymorphs of $(In_{1-x}M_x)MO_3$. *J. Am. Chem. Soc.* **2011**, *133*, 9405-9412.

(68). Frost, D. J.; Poe, B. T.; Trønnes, R. G.; Liebske, C.; Duba, A.; Rubie, D. C. A New Large-Volume Multianvil System. *Phys. Earth Planet. Inter.* **2004**, *143–144*, 507-514.

(69). Ovsyannikov, S. V.; Zainulin, Y. G.; Kadyrova, N. I.; Tyutyunnik, A. P.; Semenova, A. S.; Kasinathan, D.; Tsirlin, A. A.; Miyajima, N.; Karkin. A. E. New Antiferromagnetic Perovskite $CaCo_3V_4O_{12}$ Prepared at High-Pressure High-Temperature Conditions. *Inorg. Chem.* **2013**, *52*, 11703-11710.

(70). Ovsyannikov, S. V.; Bykova, E.; Pakhomova, A.; Kozlenko, D. P.; Bykov, M.; Kichanov, S. E.; Morozova, N. V.; Korobeinikov, I. V.; Wilhelm, F.; Rogalev, A.; Tsirlin, A. A.; Kurnosov, A. V.; Zainulin, Y. G.; Kadyrova, N. I.; Tyutyunnik, A. P.; Dubrovinsky, L. Structural and Magnetic Transitions in $CaCo_3V_4O_{12}$ Perovskite at Extreme Conditions. *Inorg. Chem.* **2017**, *56*, 6251–6263.

(71). Sheldrick, G. M. SHELXT–Integrated Space-Group and Crystal-Structure Determination. *Acta Crystallogr. A* **2015**, *71*, 3–8.

(72). Petříček, V.; Dušek, M.; Plášil, J. Crystallographic Computing System Jana2006: Solution and Refinement of Twinned Structures. *Z. Kristallogr. - Cryst. Mater.* **2016**, *231*, 583–599.

(73). Brese, N. E.; O'Keffee, M. Bond-Valence Parameters for Solids. *Acta Cryst.* **1991**, *B47*, 192-197.

(74). Rogalev, A.; Goulon, J.; Goulon-Ginet, C.; Malgrange, C., Instrumentation Developments for Polarization Dependent X-ray Spectroscopies. Magnetism and Synchrotron Radiation; Springer: Berlin, 2001; pp 60−86.

(75). Shchennikov, V. V.; Ovsyannikov, S. V.; Derevskov, A. Y.; Shchennikov, Vs. V. Automated Portable High-Pressure Setup for Study of Phase Transitions in Solids. *J. Phys. Chem. Solids* **2006**, *67*, 2203-2209.

(76). Morozova, N. V.; Korobeinikov, I. V.; Kurochka, K. V.; Titov, A. N.; Ovsyannikov, S. V. Thermoelectric Properties of Compressed Titanium and Zirconium Trichalcogenides, *J. Phys. Chem. C* **2018**, *122*, 14362–14372.

(77). Morozova, N. V.; Shchennikov, V. V.; Ovsyannikov, S. V. Features and Regularities in Behavior of Thermoelectric Properties of Rare-Earth, Transition and Other Metals under High Pressure up to 20 GPa. *J. Appl. Phys.* **2015**, *118*, 225901.

(78). Koepernik, K.; Eschrig, H. Full-potential Nonorthogonal Local-Orbital Minimum-Basis Band-Structure Scheme. *Phys. Rev. B* **1999**, *59*, 1743.

(79). Perdew, J. P.; Burke, K.; Ernzerhof, M. Generalized Gradient Approximation Made Simple. *Phys. Rev. Lett.* **1996**, *77*, 3865.

(80). Franchini, C.; Podloucky, R.; Paier, J.; Marsman, M.; Kresse, G. Ground-State Properties of Multivalent Manganese Oxides: Density Functional and Hybrid Density Functional Calculations. *Phys. Rev. B* **2007**, *75*, 195128.

(81). Kidoh, K.; Tanaka, K.; Marumo, F.; Takei, H. Electron Density Distribution in Ilmenite-Type Crystals. II. Manganese(II) Titanium(IV) Trioxide. *Acta Cryst.* **1984**, *B40*, 329-332.

(82). Katayama-Yoshida, H.; Zunger, A. Exchange-Correlation-Induced Negative Effective *U*. *Phys. Rev. Lett.* **1985**, *55*, 1618.

(83). Katayama-Yoshida, H.; Kusakabe, K.; Kizaki, H.; Nakanishi, A. General Rule and Materials Design of Negative Effective *U* System for High-T_c Superconductivity. *Appl. Phys. Express* **2008**, *1*, 081703.

(84). Ovsyannikov, S. V.; Wu, X.; Karkin, A. E.; Shchennikov, V. V.; Manthilake, G. M. Pressure-Temperature Phase Diagram of Ti_2O_3 and Physical Properties in the Golden Th_2S_3-Type Phase. Phys. Rev. B 2012, 86, 024106.

(85). Mukherjee, G. D.; Vaidya, S. N.; Karunakaran, C. High Pressure and High Temperature Studies on Manganese Oxides. *Phase Transitions* **2002**, *75*, 557–566.

(86). Geller, S.; Cape, J. A.; Grant, R. W.; Espinosa, G. P. Distortion in the Crystal Structure of α-Mn_2O_3. *Phys. Lett. A* **1967**, *24*, 369-371.

(87). Gui, Z.; Fan, R.; Chen, X.-H.; Y.-C. Wu, A Simple Direct Preparation of Nanocrystalline γ-Mn_2O_3 at Ambient Temperature. *Inorg. Chem. Comm.* **2001**, *4*, 294-296.

(88). He, W. L.; Zhang, Y. C.; Zhang, X. X.; Wang, H.; Yan, H. Low Temperature Preparation of Nanocrystalline Mn_2O_3 via Ethanol-Thermal Reduction of MnO_2. *J. Crystal Growth* **2003**, *252*, 285–288.

(89). Yamanaka, T.; Nagai, T.; Okada, T.; Fukuda, T. Structure Change of Mn_2O_3 under High Pressure and Pressure-Induced Transition. *Z. Kristallogr.* **2005**, *220*, 938–945.

(90). Shim, S.-H.; LaBounty, D.; Duffy, T. S. Raman Spectra of Bixbyite, Mn_2O_3, up to 40 GPa. *Phys. Chem. Miner.* **2011**, *38*, 685-691.

(91). Leinenweber, K.; Utsumi, W.; Tsuchida, Y.; Yagi, T.; Kurita, K. Unquenchable High-Pressure Perovskite Polymorphs of $MnSnO_3$ and $FeTiO_3$. *Phys. Chem. Miner.* **1991**, *18*, 244-250.

(92). Wu, X.; Steinle-Neumann, G.; Narygina, O.; McCammon, C.; Dubrovinsky, L. *In situ* High-Pressure Study of $LiNbO_3$-type $FeTiO_3$: X-ray Diffraction and Mössbauer Spectroscopy. *High Press. Res.* **2010**, *30*, 395-405.

(93). Chalmin, E.; Farges, F.; Brown Jr, G. E. A Pre-Edge Analysis of Mn K-edge XANES Spectra to Help Determine the Speciation of Manganese in Minerals and Glasses. *Contrib. Mineral. Petrol.* **2009**, *157*, 111–126.

(94). Yamamoto, T. Assignment of Pre-Edge Peaks in K-edge X-ray Absorption Spectra of 3d Transition Metal Compounds: Electric Dipole or Quadrupole? *X-Ray Spectrom.* **2008**, *37*, 572–584.

(95). Manceau, A.; Marcus, M. A.; Grangeon, S. Determination of Mn Valence States in Mixed-Valent Manganates by XANES Spectroscopy. *Amer. Miner.* **2012**, *97*, 816–827.

(96). Gao, P.; Metz, P.; Hey, T.; Gong, Y.; Liu, D.; Edwards, D. D.; Howe, J. Y.; Huang, R.; Misture, S. T. The Critical Role of Point Defects in Improving the Specific Capacitance of δ-MnO_2 Nanosheets. *Nat. Commun.* **2017**, *8*, 14559.

(97). Dragomir, M.; Dube, P. A.; Arčon, I.; Boyer, C.; Rutherford, M.; Wiebe, C. R.; King, G.; Dabkowska, H. A.; Greedan, J. E. Comparing Magnetism in Isostructural Oxides $A_{0.8}La_{1.2}MnO_{4.1}$: Anisotropic Spin Glass (A = Ba) versus Long-Range Order (A = Sr). *Chem. Mater.* **2019**, *31*, 7833–7844.

(98). Sharrouf, M.; Awad, R.; Roumié, M.; Marhaba, S. Structural, Optical and Room Temperature Magnetic Study of Mn_2O_3 Nanoparticles. *Materials Sciences and Applications* **2015**, *6*, 850-859.

(99). Dakhel, A. A. Correlated Structural and Electrical Properties of Thin Manganese Oxide Films. *Thin Solid Films* **2006**, *496*, 353-359.

(100). Logothetis, M.; Park, K. The Electrical Conductivity of Mn_3O_4. *Solid State Comm.* **1975**, *16*, 909.

(101). Dung, D. D; Van Thiet, D.; Tuan, D. A.; Cho, S. Strain Effects in Epitaxial Mn_2O_3 Thin Film Grown on MgO(100). *J. Appl. Phys.* **2013**, *113*, 17A314.

For Table of Contents Only

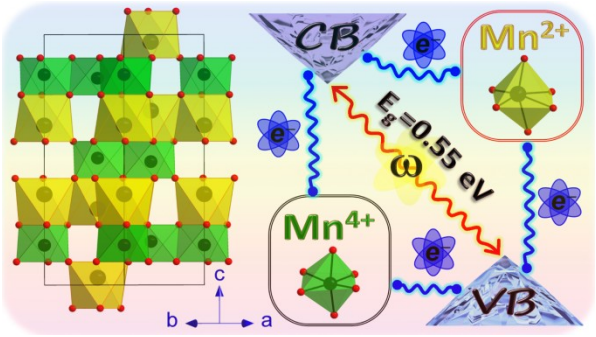

A novel ilmenite-type ε-$Mn^{2+}Mn^{4+}O_3$ phase with two different oxidation states of octahedrally-coordinated manganese cations was synthesized at high-pressure high-temperature conditions. This polymorph has a narrow indirect band gap of 0.55 eV and shows an antiferromagnetic ordering below 210 K. This finding indicates that due to charge disproportionation, binary transition metal oxides can potentially form various mixed-valence polymorphs.